

Twisted magnon as a magnetic tweezer

Y. Jiang¹, H. Y. Yuan², Z.-X. Li¹, Zhenyu Wang¹, H. W. Zhang¹, Yunshan Cao¹, and Peng Yan^{1*}

¹*School of Electronic Science and Engineering and State Key Laboratory of Electronic Thin Films and Integrated Devices, University of Electronic Science and Technology of China, Chengdu 610054, China and*

²*Department of Physics, Southern University of Science and Technology, Shenzhen 518055, China*

Wave fields with spiral phase dislocations carrying orbital angular momentum (OAM) have been realized in many branches of physics, such as for photons, sound waves, electron beams, and neutrons. However, the OAM states of magnons (spin waves)—the building block of modern magnetism—and particularly their implications have yet to be addressed. Here, we theoretically investigate the twisted spin-wave generation and propagation in magnetic nanocylinders. The OAM nature of magnons is uncovered by showing that the spin-wave eigenmode is also the eigenstate of the OAM operator in the confined geometry. Inspired by optical tweezers, we predict an exotic “magnetic tweezer” effect by showing skyrmion gyrations under twisted magnons in exchange coupled nanocylinder/nanodisk heterostructure, as a practical demonstration of magnonic OAM to manipulate topological spin defects. Our study paves the way for the emerging magnetic manipulations by harnessing the OAM degree of freedom of magnons.

Introduction.—In the past decades, the quantized orbital angular momentum (OAM) of wave fields with spatially twisted phase structure has been widely investigated as an additional degree of freedom for both fundamental and applied physics, ranging from photons [1–11], electron beams [12–18], and acoustic waves [19–25] to neutrons [26, 27] and gluons [28]. The OAM is associated with rotation of a (quasi-)particle about a fixed axis, and is encoded in the spiral phase profile of the particle’s wavefunction characterized by an azimuthal ϕ phase dependence $e^{i\ell\phi}$ with a nonzero topological charge ℓ (an integer) and a vanishing field at the core. The OAM component in the direction of rotational axis has the quantized value $\ell\hbar$ with \hbar the reduced Planck constant, in contrast to the spin angular momentum (SAM) originating from the wave polarization. Such twisted OAM states have a phase dislocation on the axis that is sometimes referred to as an (optical, acoustic, and/or electron) vortex. When interactions of the particle with its environment are of a rotational symmetry, OAM is conserved. Vortices with high OAM can be achieved using spiral phase plates, computer-generated holograms, mode conversions, and spatial modulators, among others. However, the OAM state of magnons (or spin waves)—as elementary excitations in ordered magnets—has received little attention by the community [29, 30] and its practical implication has never been addressed, although their linear momentum and SAM degrees of freedom have been extensively explored in the context of Brillouin light scattering spectroscopy [31], magnon-driven dynamics of topological spin texture [32–36], Bose-Einstein magnon condensation [37], etc.

In this Letter, we uncover the OAM nature of magnons by studying the spin-wave dynamics in magnetic nanocylinders (see Fig. 1). As a proof of concept, we generate magnon beams carrying OAM quantum number $|\ell| \leq +8$ via a localized spatiotemporal field. Inspired by the notion of optical tweezers [38], we predict a “magnetic tweezer” effect by demonstrating twisted-magnon induced skyrmion gyration in a chiral magnetic nanodisk exchange-coupled to one end of the magnetic nanocylinder, as a practical application of the magnonic OAM transfer to matter.

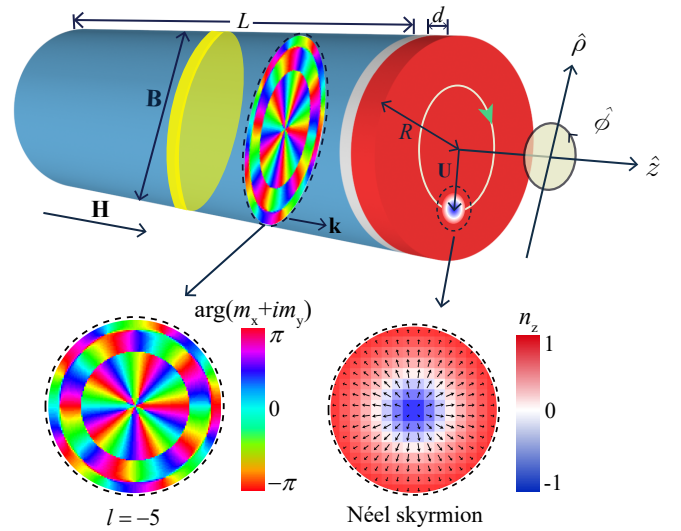


FIG. 1: Schematic illustration of a heterostructured nanocylinder exchange-coupled to a chiral magnetic nanodisk hosting a Néel-type skyrmion. An external static field \mathbf{H} is applied along the z -direction. A spin-wave beam with the wavevector \mathbf{k} and OAM quantum number $\ell = -5$ is excited by a localized microwave field \mathbf{B} , leading to a steady skyrmion gyration around the disk center.

OAM of twisted magnons.—We start with the following Hamiltonian modelling a uniaxial ferromagnet of the cylindrical geometry (see Fig. 1 supposing $L \rightarrow \infty$),

$$\mathcal{H} = \int d\mathbf{r} \left[\frac{A}{M_s^2} (\nabla \mathbf{M})^2 - \mu_0 \mathbf{M} \cdot (\mathbf{H} + \mathbf{h}) \right], \quad (1)$$

where $\mathbf{M} = M_s \mathbf{m}$ is the local magnetization with the saturated value M_s and the direction \mathbf{m} , A is the exchange constant, $\mathbf{H} = H_0 \hat{z}$ is the external field along the z -axis (the symmetry axis of the cylinder), μ_0 is the vacuum permeability, and \mathbf{h} is the dipolar field satisfying the magnetostatic equation $\nabla \times \mathbf{h}(\mathbf{r}, t) = 0$ and $\nabla \cdot [\mathbf{h}(\mathbf{r}, t) + M_s \mathbf{m}(\mathbf{r}, t)] = 0$. We therefore have $\mathbf{h}(\mathbf{r}, t) = -\nabla \Phi(\mathbf{r}, t)$ where Φ is a magnetostatic potential. The spatiotemporal evolution of magnetization is governed by

the classical Landau-Lifshitz-Gilbert (LLG) equation,

$$\frac{\partial \mathbf{m}}{\partial t} = -\gamma \mu_0 \mathbf{m} \times \mathbf{H}_{\text{eff}} + \alpha \mathbf{m} \times \frac{\partial \mathbf{m}}{\partial t}, \quad (2)$$

where $\gamma = 2.8 \times 10^{10}$ Hz/T is the gyromagnetic ratio, α is the dimensionless Gilbert damping constant, and $\mathbf{H}_{\text{eff}} = -\mu_0^{-1} \delta \mathcal{H} / \delta \mathbf{M} = H_0 \hat{z} + \mathbf{h}(\mathbf{r}, t) + \frac{2A}{\mu_0 M_s} \nabla^2 \mathbf{m}(\mathbf{r}, t)$ is the effective magnetic field. We consider the spin wave excitation on top of a uniform magnetization: $\mathbf{m} = (m_x, m_y, 1)$ with $m_x^2 + m_y^2 \ll 1$. We pursue the time-harmonic solution and write the field variables in a product form: $m_{x(y)}(\mathbf{r}, t) = m_{x(y)}(\mathbf{r}) e^{-i\omega t}$ and $\Phi(\mathbf{r}, t) = \Phi(\mathbf{r}) e^{-i\omega t}$ with the frequency ω . Substituting these terms into the coupled magnetostatic and LLG equations and adopting the linear approximation, we obtain

$$i\bar{\omega} m_x = (H_0 - \bar{A} \nabla^2) m_y + \frac{\partial \Phi}{\partial y}, \quad (3a)$$

$$-i\bar{\omega} m_y = (H_0 - \bar{A} \nabla^2) m_x + \frac{\partial \Phi}{\partial x}, \quad (3b)$$

$$\nabla^2 \Phi = M_s \left(\frac{\partial m_x}{\partial x} + \frac{\partial m_y}{\partial y} \right), \quad (3c)$$

with $\bar{\omega} = \omega / (\gamma \mu_0)$ and $\bar{A} = 2A / (\mu_0 M_s)$. In cylindrical coordinates, the magnetic potential within the cylinder takes the form $\Phi(\rho, \phi, z) \sim J_n(\kappa \rho) e^{in\phi + ikz}$. Here, $J_n(\kappa \rho)$ is the Bessel function of the first kind, $n = 0, \pm 1, \pm 2, \dots$ is the azimuthal quantum number, k is the longitudinal wave number, and κ is the transverse wave number. Substituting the Bessel profile into Eqs. (3) leads to the following dispersion relation: $-H_0 M_s k^2 + [H_0(H_0 + M_s) - \bar{\omega}^2 - \bar{A} M_s k^2](\kappa^2 + k^2) + \bar{A}(2H_0 + M_s)(\kappa^2 + k^2)^2 + \bar{A}^2(\kappa^2 + k^2)^3 = 0$ which is cubic in κ^2 , so that for each combination of ℓ and k , we have three linearly independent solutions of the magnetic potential $\Phi(\rho, \phi, z) = \sum_{j=1}^3 c_j J_n(\kappa_j \rho) e^{i(n\phi + kz)}$ for $\rho \leq R$ and $\Phi(\rho, \phi, z) = c_4 K_n(k\rho) e^{i(n\phi + kz)}$ for $\rho > R$, where $K_n(k\rho)$ is the modified Bessel function of the second kind. Accordingly, the radial and azimuthal components of the dynamical magnetization are given by $m_\rho(\rho, \phi, z) = \frac{1}{2} \sum_j^3 c_j \kappa_j \left[\frac{J_{n+1}(\kappa_j \rho)}{\bar{A}(\kappa_j^2 + k^2) + H_0 + \bar{\omega}} - \frac{J_{n-1}(\kappa_j \rho)}{\bar{A}(\kappa_j^2 + k^2) + H_0 - \bar{\omega}} \right] e^{i(n\phi + kz)}$, $m_\phi(\rho, \phi, z) = \frac{-i}{2} \sum_j^3 c_j \kappa_j \left[\frac{J_{n+1}(\kappa_j \rho)}{\bar{A}(\kappa_j^2 + k^2) + H_0 + \bar{\omega}} + \frac{J_{n-1}(\kappa_j \rho)}{\bar{A}(\kappa_j^2 + k^2) + H_0 - \bar{\omega}} \right] e^{i(n\phi + kz)}$, in which we have defined $m_\rho = \cos \phi m_x + \sin \phi m_y$ and $m_\phi = -\sin \phi m_x + \cos \phi m_y$. According to Noether's theorem, one can derive the OAM density of twisted magnons

$$\mathcal{J}_z = \frac{\hbar}{S} \iint (\nabla \psi \times \mathbf{r})_z dx dy, \quad (4)$$

where $S = \pi R^2$ is the cross-section area of the nanocylinder and $\psi(\mathbf{r}) = \arg(m_x + im_y)$ [30]. Substituting the dynamical magnetization profile into Eq. (4), we obtain $\mathcal{J}_z = \ell \hbar$ with $\ell = n - 1$, the quantized OAM per twisted magnon.

The determination of the four unknown parameters c_1, c_2, c_3 , and c_4 depends on the boundary conditions on the

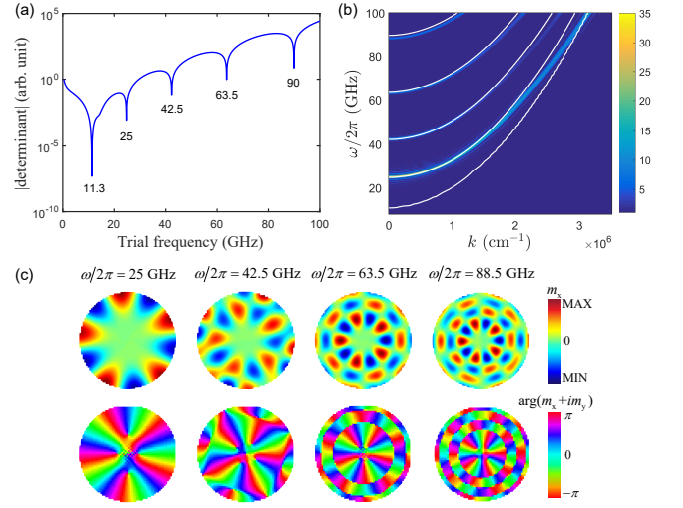


FIG. 2: (a) Boundary-value determinant versus trial frequencies for a longitudinal wavevector $k = 1 \times 10^5 \text{ cm}^{-1}$ and $\ell = -5$. (b) Spin-wave spectrum in the nanocylinder. Solid curves are theoretical results, comparing with the FFT spectrum from micromagnetic simulations. (c) Cross-sectional distribution of spin-wave beams with 0, 1, 2, and 3 radial nodes (from left to right).

nanocylinder surface

$$\sum_{j=1}^3 c_j J_n(\kappa_j R) = c_4 K_n(kR), \quad (5a)$$

$$-\sum_{j=1}^3 c_j \partial_\rho J_n(\kappa_j \rho)|_{\rho=R} + M_s m_\rho|_{\rho=R} = -c_4 \partial_\rho K_n(k\rho)|_{\rho=R}, \quad (5b)$$

$$(\partial_\rho m_\rho - \zeta m_\rho)|_{\rho=R} = 0, \quad \partial_\rho m_\phi|_{\rho=R} = 0, \quad (5c)$$

where ζ is the pinning parameter due to the surface anisotropy [39]. There is no surface spin pinning when $\zeta = 0$, whereas the surface spins are fully pinned if ζ is sufficiently large. We are interested in free boundaries in following calculations. Equations (5) allow us writing the condition for the existence of nontrivial solutions

$$\det \Delta(\bar{\omega}, \kappa_1, \kappa_2, \kappa_3) = 0, \quad (6)$$

where $\Delta(\bar{\omega}, \kappa_j)$ is the 4×4 coefficient matrix of Eq. (5). It is unlikely to derive an analytical expression of the spin-wave spectrum by solving Eq. (6) because of the algebraic complexity. In what follows, we shall solve the problem numerically by searching for zeros of the magnitude of the determinant Δ within a preset accuracy [40].

We consider an isolated yttrium iron garnet (YIG) nanocylinder of length $L = 2 \mu\text{m}$ and radius $R = 60 \text{ nm}$ [41]. The external static magnetic field is $\mu_0 H_0 = 0.4 \text{ T}$. We consider the case where the azimuthal quantum number $\ell = -5$. In Fig. 2(a), we show the magnitude of the determinant Δ as a function of trial frequencies for $k = 1 \times 10^5 \text{ cm}^{-1}$. Below 100 GHz, we find five frequencies at 11.3, 25, 42.5, 63.5, and 90 GHz satisfying boundary conditions. Full band structure is plotted by white curves in Fig. 2(b) through system-

atically varying k . To verify the theoretical spin-wave spectrum, we simulate the LLG equation (2) using the micromagnetic codes MuMax3 [42]. To excite higher-order spin-wave modes, we apply a microwave driving field of sinc-function $\mathbf{B} = B_s \frac{\sin \omega_B t}{\omega_B t} (\cos \ell \phi, -\sin \ell \phi, 0)$ for 2 ns with $B_s = 0.3$ T, $\ell = -5$, and $\omega_B/2\pi = 100$ GHz, over a 12 nm thick region in the middle of the nanowire which is discretized using the cell size of $2 \times 2 \times 1$ nm³. The spatiotemporal oscillation of m_x is analyzed over lattices of wire axis. The corresponding fast Fourier transformation (FFT) spectrum is plotted in Fig. 2(b). Simulation results compare well with theoretical curves, except the lowest band which represents the cross-sectionally uniform spin-wave mode and cannot be generated by an inhomogeneous microwave field. Figure 2(c) shows the cross-sectional distribution of different modes emerging in Fig. 2(a), from which we find that these modes actually have 0, 1, 2, and 3 radial nodes, viewed from left to right, respectively. We focus on the twisted magnons with 2 nodes [the 2nd white curve in Fig. 2(b) by seeing from above] since they are ideal for trapping topological spin defects, e.g., magnetic skyrmions and vortices.

Magnetic tweezer effect.—To illustrate how twisted magnons can manipulate magnetic textures, we consider a heterostructure shown in Fig. 1. The nanodisk is a chiral ferromagnet containing a stabilized skyrmion. Twisted magnons are excited in the YIG nanocylinder and then propagate rightward ($+\hat{z}$) to interact with the skyrmion in the nanodisk, through an interfacial exchange coupling. Here, the magnetization dynamics in the nanodisk is described by LLG equation with an extra torque as

$$\frac{\partial \mathbf{n}}{\partial t} = -\gamma \mu_0 \mathbf{n} \times (\mathbf{H}'_{\text{eff}} + \mathbf{H}_{\text{ex}}) + \alpha' \mathbf{n} \times \frac{\partial \mathbf{n}}{\partial t}, \quad (7)$$

where \mathbf{n} is the unit vector of local magnetization in the nanodisk, \mathbf{H}'_{eff} is the effective field, \mathbf{H}_{ex} is an interfacial field resulting from the nanocylinder|nanodisk exchange coupling, and α' is the Gilbert damping. Generally, the exchange coupling takes the form $E_{\text{ex}} = -J_{\text{ex}} \mathbf{n}(\mathbf{r}, t) \cdot \mathbf{m}(\mathbf{r}, t)$ such that $\mathbf{H}_{\text{ex}} = J_{\text{ex}} \mathbf{m}(\mathbf{r}, t)/(\mu_0 M'_s)$. In this sense, an extra exchange field $\tilde{\mathbf{H}}_{\text{ex}} = J_{\text{ex}} \mathbf{n}(\mathbf{r}, t)/(\mu_0 M'_s)$ should also be supplemented into Eq. (2) to correctly model the YIG dynamics. Via the interfacial exchange coupling, twisted magnons can transfer their OAM to skyrmions (we omit the spin-wave reflection at the interface). One thus expects a circular skyrmion motion, because a gyrating skyrmion manifests itself carrying OAM as well [11]. Below we address this idea analytically and numerically.

We adopt the generalized Thiele's model to make analytical predictions. By performing $[\mathbf{n} \times \text{Eq. (7)}] \cdot \nabla \mathbf{n}$ and considering the steady skyrmion motion $\mathbf{n}(\mathbf{r}, t) = \mathbf{n}[\mathbf{r} - \mathbf{U}(t)]$, we obtain

$$\mathcal{G} \hat{z} \times \frac{d\mathbf{U}}{dt} - \alpha' \mathcal{D} \cdot \frac{d\mathbf{U}}{dt} + \mathbf{F} = 0, \quad (8)$$

where \mathbf{U} is the displacement of the skyrmion core from the origin of coordinate; $\mathcal{G} = -4\pi Q d M'_s / \gamma$ is the gyroscopic constant with $Q = \frac{1}{4\pi} \iint \mathbf{n} \cdot (\frac{\partial \mathbf{n}}{\partial x} \times \frac{\partial \mathbf{n}}{\partial y}) dx dy$ being the topological

charge [$Q = -1$ for the skyrmion configuration shown in Fig. 1] and the integral region being confined in the nanodisk; d is the thickness of the nanodisk; M'_s is the saturation magnetization; and $\mathcal{D}_{ij} = (dM'_s/\gamma) \iint \partial_i \mathbf{n} \cdot \partial_j \mathbf{n} dx dy$ is the dissipation tensor. The driving force includes two parts $\mathbf{F} = \mathbf{f} + \mathbf{g}$, where $\mathbf{f}(t) = -\mathcal{K}_0 \mathbf{U}(t)$ is the restoring force from disk boundary with the positive spring constant $\mathcal{K}_0 \propto 1/R^4$ [43], and $\mathbf{g}_t(\mathbf{U}(t), t) = J_{\text{ex}} d \iint \mathbf{m}(\mathbf{r}, t) \cdot \partial_i \mathbf{n}[\mathbf{r} - \mathbf{U}(t)] dx dy$ is the force due to twisted magnons from the nanocylinder. Typically, the skyrmion dynamics is much slower than the spin-wave precession, i.e., $|\dot{\mathbf{U}}(t)|/U(t) \ll |\dot{\mathbf{m}}|$ with $U(t) = |\mathbf{U}(t)|$. The \mathbf{g} force can thus be divided into two terms $\mathbf{g} = \mathbf{g}'[\mathbf{U}(t)] + \mathbf{g}''(t)$. Here, \mathbf{g}' is the slow component with the same time-scale as the skyrmion guiding center, whereas \mathbf{g}'' evolves as fast as the twisted magnons and $\langle \mathbf{g}'' \rangle = 0$ by coarse-graining. Considering the leading-order terms only, we can expand the total driving-force as

$$\mathbf{F} = -\mathcal{K} \mathbf{U}(t) - \lambda \hat{\phi}, \quad (9)$$

where $\mathcal{K} = \mathcal{K}_0 + \Delta \mathcal{K}$ is the effective spring constant with $\Delta \mathcal{K}$ contributed by twisted magnons and λ is the coefficient of azimuthal force. We note that both $\Delta \mathcal{K}$ and λ are (approximately) odd functions of the OAM quantum number ℓ . In a large-sized nanodisk, $\Delta \mathcal{K}$ can dominate over \mathcal{K}_0 . By seeking the steady-state solution for skyrmion gyrations, i.e., $U = \text{const.}$, and substituting (9) into (8), we obtain

$$\dot{\mathbf{U}}(t) = -\frac{\mathcal{K}U}{\mathcal{G}} \hat{\phi}, \quad \text{and } U = \frac{\lambda \mathcal{G}}{\alpha' \mathcal{K} \mathcal{D}}. \quad (10)$$

The above result uncovers the two-fold contributions of twisted magnons in driving the skyrmion motion: On the one hand, it induces an extra confining force which determines the gyration frequency of the circular motion. On the other hand, it generates an azimuthal force to compensate the dissipation to sustain a stable gyration and prevent the skyrmion from falling into the disk center. Under a suitable orbit radius U , these two physical processes reach a balance. Because the spring model with constant coefficients is exact only when $U/R \ll 1$ [43], both \mathcal{K} and λ may depend on the orbit radius U [see Fig. 4(c)]. It is also difficult to analytically derive the complex ℓ -dependence of these two parameters. To verify our theoretical predictions, we perform full micromagnetic simulations below.

Micromagnetic simulations.—We consider a Co/Pt nanodisk [44, 45] coupled to the YIG cylinder with the exchange coefficient $J_{\text{ex}} = 2.31 \times 10^5$ J/m³. The Laguerre-Gaussian (LG) excitation microwave field $\mathbf{B}_t(\rho, \phi, t) = B_0 (\frac{\rho}{w})^{|\ell|} e^{-\frac{\rho^2}{w^2}} \mathcal{L}_2^{|\ell|}(\frac{2\rho^2}{w^2}) \cos(-\omega t + \ell \phi) \hat{x}$ is locally applied at $z = -20$ nm (we set the interface as the origin of coordinate). Here, w is the width of the beam waist, B_0 is the field amplitude, and $\mathcal{L}_2^{|\ell|}$ is the generalized Laguerre function. In the simulations, we set $w = 24.3$ nm and $B_0 = 0.26$ T. We have numerically generated twisted 2-node magnon beams with a constant wavevector $k = 1 \times 10^5$ cm⁻¹ and OAM $-8 \leq \ell \leq 0$ by varying the excitation frequency ω [see FFT analysis in

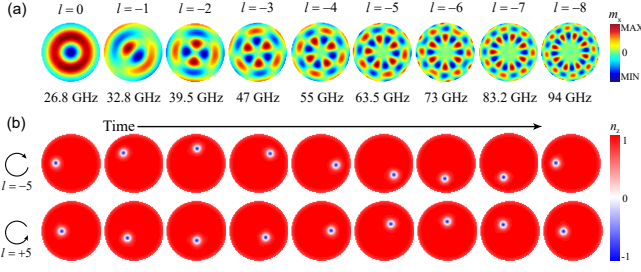


FIG. 3: (a) Cross-sectional view of numerically excited 2-node spin-wave beams carrying different OAMs. (b) Time evolution of Néel skyrmions confined in the nanodisk driven by twisted magnons with OAM $\ell = \mp 5$. The time intervals between successive snapshots in two cases are 1.65 ns and 1.98 ns, respectively. A negative (positive) OAM induces a clockwise (counterclockwise) skyrmion gyration.

Fig. 3(a)]. The excitation frequency ω monotonically increases with the OAM magnitude $|\ell|$.

Figure 3(b) shows the steady skyrmion gyration under twisted magnon beams. The initial position of skyrmion is $\mathbf{U}(t=0) = (-22, 0)$ nm [see Fig. 4(a)]. For $\ell = -5$, we observe a clockwise skyrmion circular motion with an average velocity 15.2 m/s along the orbit of radius 31.9 nm [shown in Figs. 3(b) and 4(a)]. To prove that the rotational motion is indeed due to the OAM transfer from twisted magnons to the skyrmion, we reverse the OAM of the magnon beam to $\ell = +5$ without changing the rest parameters. We then observe a counterclockwise gyration of the skyrmion, as expected. However, the skyrmion velocity is now significantly reduced to 7.82 m/s along a shrunk orbit of a radius 19.7 nm [see Figs. 3(b) and 4(c)], which can be explained by the simultaneous sign change of $\Delta\mathcal{K}$ and λ when ℓ switches from -5 to $+5$ (illustrated below). As a comparison, we consider the case with a vanishing OAM ($\ell = 0$) and find the skyrmion falling into the disk center [gray curve plotted in Fig. 4(a)], which is consistent with the OAM transfer picture.

Figure 4(b) plots the time-dependence of the guiding center $U_{x,y}$ driven by the spin-wave beam with $\ell = -5$, indicating an overall period of 13.2 ns. However, by carefully investigating the orbit, we observe a fast oscillation mode (right inset). Through the FFT analysis of $\mathbf{U}(t)$, we identify two peaks at 0.076 and 63.5 GHz (left inset), which correspond to the skyrmion gyration and spin wave precession, respectively. The relatively lower peak of the fast mode justifies our coarse-graining treatment on \mathbf{g}'' . Furthermore, we confirm the important role of damping. As shown in Fig. 4(c), the skyrmion velocity monotonically decreases with α' for $\ell = -5$. However, for $\ell = +5$ the skyrmion velocity first increases until a certain value and then decreases. We also find a shrinking (surprisingly expanding) of the gyration orbit for $\ell = -5$ ($\ell = +5$) when α' increases. To interpret these numerical observations, we derive the U -dependence of parameters \mathcal{K} and λ in Eq. (9) (see the inset), which indeed shows a sign reversal when ℓ is switched from -5 to $+5$. The orbit shrinking and expanding can thus be understood as follows: For $\ell = -5$, the spring coefficient $\mathcal{K} > 0$ and the radial force in Eq. (9) is centripetal.

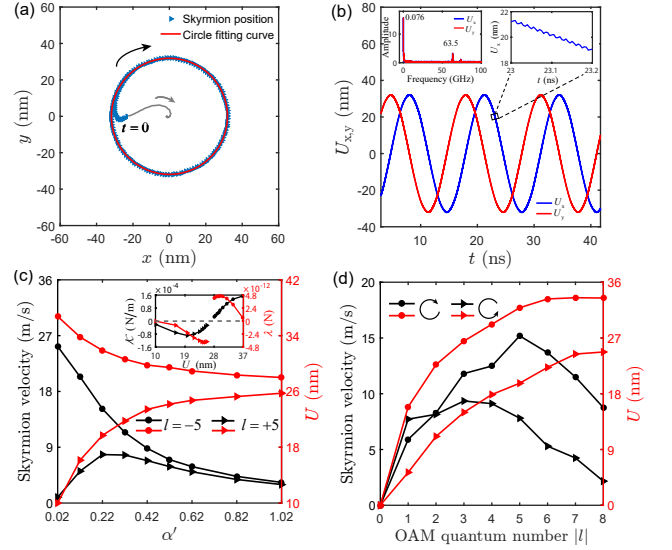


FIG. 4: (a) Skyrmion gyration path (symbols) and the circle fitting curve (red circle) for $\ell = -5$. Gray curve represents the path for $\ell = 0$. (b) Time-dependence of U_x (blue line) and U_y (red line). Inset shows the high-frequency details of the FFT spectrum (left) and U_x (right). Skyrmion velocity and orbit radius as a function of (c) damping parameter α' and (d) OAM quantum number ℓ . Inset plots the U -dependence of \mathcal{K} and λ . $\alpha' = 0.22$ is adopted for (a), (b), and (d).

efficient $\mathcal{K} > 0$ and the radial force in Eq. (9) is centripetal. An increased damping will slow down skyrmion's gyrating velocity and shrink its orbit radius. For $\ell = +5$, the spring coefficient $\mathcal{K} < 0$ and the radial force becomes centrifugal. However, the Thiele's equation (8) is invariant by transformations $\mathcal{G} \rightarrow -\mathcal{G}$, $\lambda \rightarrow -\lambda$, $\mathcal{K} \rightarrow -\mathcal{K}$, and $\alpha' \rightarrow -\alpha'$, through which the radial force recovers its centripetal nature. The $-\alpha'$ can be viewed as a gain [46], instead of damping. An increased α' thus represents an enhanced gain, which naturally leads to the expansion of gyration orbits. The non-monotonic $|\ell|$ -dependence of the skyrmion velocity indicates the possibility to optimize twisted spin-wave beams and material parameters, although a larger OAM magnitude always expands the gyration orbit, as shown in Fig. 4(d).

Discussion.—In numerical simulations, we use the LG microwave field to generate twisted magnons. From an experimental point of view, spin-wave beams carrying various OAM can be excited by Brillouin light scattering when selection rules are satisfied [47] or by magnetic spiral phase plates [48]. Very recently, twisted photons (optical vortices) are proposed to be able to drive a rotational motion of skyrmion, which however suffers from the diffraction limit and is challenging to realize [11, 49, 50]. In contrast to its photonic counterpart, the magnonic vortex matches all time- and length-scales of skyrmion dynamics, free from the mentioned limitations. Our magnonic OAM induced skyrmion velocity can reach tens of meters per second with a low power consumption. It is comparable to the current-driven skyrmion velocity in nanodisks that, however, work at very high current densities $10^{10} \sim 10^{12}$ A/m² [51, 52]. Furthermore, the OAM transfer of twisted

magnons here does not require electron transport, so that the Joule heating is, in principle, avoided. The magnonic tweezers can also find applications in manipulating other types of spin defects, such as magnetic vortex [53], bobber [54, 55], meron [56], hopfion [57–61], etc. Twisted magnons in antiferromagnets [62] may manifest themselves THz magnetic tweezers. Pushing the magnonic OAM manipulation into quantum regions [63] is also an interesting issue.

To conclude, we studied the spin-wave spectrum in magnetic nanocylinders and showed that twisted magnons carry intrinsic OAM in this confined geometry. We predicted magnonic tweezers effect by demonstrating that magnonic vortices can drive the dynamics of topological spin defects. Taking the magnetic skyrmion as an example, we showed both theoretically and numerically that twisted spin-wave beams can induce a steady-state skyrmion gyration in a hybrid nanocylinder/nanodisk structure. Our work opens the door for twisted magnonics, an emerging field about all-magnonic manipulation by harnessing the OAM of magnons, in addition to their linear momentum and SAM degrees of freedom.

This work was funded by the National Natural Science Foundation of China (Grants No. 11604041, No. 11704060, and No. 11904048), the National Key Research Development Program under Contract No. 2016YFA0300801, and the National Thousand-Young-Talent Program of China. H.Y. acknowledges financial support from the National Natural Science Foundation of China under Grant No. 61704071.

Y.J. and H.Y. contributed equally to this work.

* Corresponding author: yan@uestc.edu.cn

- [1] L. Allen, M. W. Beijersbergen, R. J. Spreeuw, and J. P. Woerdman, Orbital angular momentum of light and the transformation of Laguerre-Gaussian laser modes, *Phys. Rev. A* **45**, 8185 (1992).
- [2] L. Allen, S. M. Barnett, and M. J. Padgett, *Optical Angular Momentum* (CRC Press, Boca Raton, 2003).
- [3] *Twisted Photons: Applications of Light with Orbital Angular Momentum*, edited by J. P. Torres and L. Torner (Wiley-VCH, 2011).
- [4] *The Angular Momentum of Light*, edited by D. L. Andrews and M. Babiker (Cambridge University Press, 2012).
- [5] A. Mair, A. Vaziri, G. Weihs, and A. Zeilinger, Entanglement of the orbital angular momentum states of photons, *Nature (London)* **412**, 313 (2001).
- [6] G. Vallone, V. D'Ambrosio, A. Sponselli, S. Slussarenko, L. Marrucci, F. Sciarrino, and P. Villoresi, Free-Space Quantum Key Distribution by Rotation-Invariant Twisted Photons, *Phys. Rev. Lett.* **113**, 060503 (2014).
- [7] S. Fühapter, A. Jesacher, S. Bernet, and M. Ritsch-Marte, Spiral phase contrast imaging in microscopy, *Opt. Express* **13**, 689 (2005).
- [8] F. Tamburini, B. Thidé, G. Molina-Terriza, and G. Anzolin, Twisting of light around rotating black holes, *Nat. Phys.* **7**, 195 (2011).
- [9] D. G. Grier, A revolution in optical manipulation, *Nature (London)* **424**, 810 (2003).
- [10] P. H. Jones, O. M. Maragò, and G. Volpe, *Optical Tweezers: Principles and Applications* (Cambridge University Press, 2015).
- [11] W. Yang, H. Yang, Y. Cao, and P. Yan, Photonic orbital angular momentum transfer and magnetic skyrmion rotation, *Opt. Express* **26**, 8778 (2018).
- [12] K. Yu. Bliokh, Y. P. Bliokh, S. Savel'ev, and F. Nori, Semi-classical Dynamics of Electron Wave Packet States with Phase Vortices, *Phys. Rev. Lett.* **99**, 190404 (2007).
- [13] M. Uchida and A. Tonomura, Generation of electron beams carrying orbital angular momentum, *Nature (London)* **464**, 737 (2010).
- [14] J. Verbeeck, H. Tian, and P. Schattschneider, Production and application of electron vortex beams, *Nature (London)* **467**, 301 (2010).
- [15] B. J. McMoran, A. Agrawal, I. M. Anderson, A. A. Herzing, H. J. Lezec, J. J. McClelland, and J. Unguris, Electron Vortex Beams with High Quanta of Orbital Angular Momentum, *Science* **331**, 192 (2011).
- [16] E. Mafakheri, A. H. Tavabi, P.-H. Lu, R. Balboni, F. Venturi, C. Menozzi, G. C. Gazzadi, S. Frabboni, A. Sit, R. E. Dunin-Borkowski, E. Karimi, and V. Grillo, Realization of electron vortices with large orbital angular momentum using miniature holograms fabricated by electron beam lithography, *Appl. Phys. Lett.* **110**, 093113 (2017).
- [17] A. J. Silenko, P. Zhang, and L. Zou, Manipulating Twisted Electron Beams, *Phys. Rev. Lett.* **119**, 243903 (2017).
- [18] S. M. Lloyd, M. Babiker, G. Thirunavukkarasu, and J. Yuan, Electron vortices: Beams with orbital angular momentum, *Rev. Mod. Phys.* **89**, 035004 (2017).
- [19] J. F. Nye and M. V. Berry, Dislocations in wave trains, *Proc. R. Soc. A* **336**, 165 (1974).
- [20] B. T. Hefner and P. L. Marston, Dislocations in wave trains, *J. Acoust. Soc. Am.* **106**, 3313 (1999).
- [21] A. Anhäuser, R. Wunenburger, and E. Brasselet, Acoustic Rotational Manipulation Using Orbital Angular Momentum Transfer, *Phys. Rev. Lett.* **109**, 034301 (2012).
- [22] Z. Hong, J. Zhang, and B. W. Drinkwater, Observation of Orbital Angular Momentum Transfer from Bessel-Shaped Acoustic Vortices to Diphasic Liquid-Microparticle Mixtures, *Phys. Rev. Lett.* **114**, 214301 (2015).
- [23] A. Marzo, M. Caleap, and B. W. Drinkwater, Acoustic Virtual Vortices with Tunable Orbital Angular Momentum for Trapping of Mie Particles, *Phys. Rev. Lett.* **120**, 044301 (2018).
- [24] D. Baresch, J.-L. Thomas, and R. Marchiano, Orbital Angular Momentum Transfer to Stably Trapped Elastic Particles in Acoustical Vortex Beams, *Phys. Rev. Lett.* **121**, 074301 (2018).
- [25] L. Zhang, Reversals of Orbital Angular Momentum Transfer and Radiation Torque, *Phys. Rev. Applied* **10**, 034039 (2018).
- [26] C. W. Clark, R. Barankov, M. G. Huber, M. Arif, D. G. Cory, and D. A. Pushin, Controlling neutron orbital angular momentum, *Nature (London)* **525**, 504 (2015).
- [27] R. L. Cappelletti, T. Jach, and J. Vinson, Intrinsic Orbital Angular Momentum States of Neutrons, *Phys. Rev. Lett.* **120**, 090402 (2018).
- [28] X. Ji, F. Yuan, and Y. Zhao, Hunting the Gluon Orbital Angular Momentum at the Electron-Ion Collider, *Phys. Rev. Lett.* **118**, 192004 (2017).
- [29] V. M. Tsukernik, Some features of the gyromagnetic effect in ferroelectrics at low temperatures, *Zh. Eksp. Teor. Fiz.* **50**, 1631 (1966) [*Sov. Phys. JETP* **23**, 1085 (1966)].
- [30] P. Yan, A. Kamra, Y. Cao, and G. E. W. Bauer, Angular and linear momentum of excited ferromagnets, *Phys. Rev. B* **88**, 144413 (2013).

- [31] S. O. Demokritov, B. Hillebrands, and A. N. Slavin, Brillouin light scattering studies of confined spin waves: linear and non-linear confinement, *Phys. Rep.* **348**, 441 (2001).
- [32] P. Yan, X. S. Wang, and X. R. Wang, All-Magnonic Spin-Transfer Torque and Domain Wall Propagation, *Phys. Rev. Lett.* **107**, 177207 (2011).
- [33] W. Jiang, P. Upadhyaya, Y. Fan, J. Zhao, M. Wang, L.-T. Chang, M. Lang, K. L. Wong, M. Lewis, Y.-T. Lin, J. Tang, S. Cherepov, X. Zhou, Y. Tserkovnyak, R. N. Schwartz, and K. L. Wang, Direct Imaging of Thermally Driven Domain Wall Motion in Magnetic Insulators, *Phys. Rev. Lett.* **110**, 177202 (2013).
- [34] X.-G. Wang, G.-H. Guo, Y.-Z. Nie, G.-F. Zhang, and Z.-X. Li, Domain wall motion induced by the magnonic spin current, *Phys. Rev. B* **86**, 054445 (2012).
- [35] W. Wang, M. Albert, M. Beg, M.-A. Bisotti, D. Chernyshenko, D. Cortés-Ortuño, I. Hawke, and H. Fangohr, Magnon-Driven Domain-Wall Motion with the Dzyaloshinskii-Moriya Interaction, *Phys. Rev. Lett.* **114**, 087203 (2015).
- [36] S.-Z. Lin, C. Reichhardt, C. D. Batista, and A. Saxena, Driven Skyrmions and Dynamical Transitions in Chiral Magnets, *Phys. Rev. Lett.* **110**, 207202 (2013).
- [37] S. O. Demokritov, V. E. Demidov, O. Dzyapko, G. A. Melkov, A. A. Serga, B. Hillebrands, and A. N. Slavin, Bose-Einstein condensation of quasi-equilibrium magnons at room temperature under pumping, *Nature (London)* **443**, 430 (2006).
- [38] A. Ashkin, J. M. Dziedzic, J. E. Bjorkholm, and S. Chu, Observation of a single-beam gradient force optical trap for dielectric particles, *Opt. Lett.* **11**, 288 (1986).
- [39] A. G. Gurevich and G. A. Melkov, *Magnetization Oscillations and Waves* (CRC Press, Boca Raton, 1996).
- [40] See Chap. 31 in *Handbook of Nanophysics: Nanotubes and Nanowires*, edited by K. D. Sattler (CRC Press, Boca Raton, 2011).
- [41] The following magnetic parameters are used for YIG: saturation magnetization $M_s = 1.92 \times 10^5$ A/m, exchange constant $A = 3.1 \times 10^{-12}$ J/m, and Gilbert damping $\alpha = 4 \times 10^{-4}$.
- [42] A. Vansteenkiste, J. Leliaert, M. Dvornik, M. Helsen, F. Garcia-Sanchez, and B. Van Waeyenberge, The design and verification of MuMax3, *AIP Adv.* **4**, 107133 (2014).
- [43] H. Yang, C. Wang, X. Wang, X. S. Wang, Y. Cao, and P. Yan, Twisted skyrmions at domain boundaries and the method of image skyrmions, *Phys. Rev. B* **98**, 014433 (2018).
- [44] We adopted the following magnetic parameters for Co/Pt [45]: nanodisk thickness $d = 1$ nm, saturation magnetization $M'_s = 5.8 \times 10^5$ A/m, exchange constant $A' = 1.5 \times 10^{-11}$ J/m, uniaxial anisotropy $K_u = 8 \times 10^5$ J/m³, interfacial Dzyaloshinskii-Moriya constant $D = 3.7 \times 10^{-3}$ J/m², and damping coefficient $\alpha' = 0.22$ unless otherwise stated.
- [45] J. Sampaio, V. Cros, S. Rohart, A. Thiaville, and A. Fert, Nucleation, stability and current-induced motion of isolated magnetic skyrmions in nanostructures, *Nat. Nano.* **8**, 839 (2013).
- [46] H. Yang, C. Wang, T. Yu, Y. Cao, and P. Yan, Antiferromagnetism Emerging in a Ferromagnet with Gain, *Phys. Rev. Lett.* **121**, 197201 (2018).
- [47] J. A. Haigh, N. J. Lambert, S. Sharma, Y. M. Blanter, G. E. W. Bauer, and A. J. Ramsay, Selection rules for cavity-enhanced Brillouin light scattering from magnetostatic modes, *Phys. Rev. B* **97**, 214423 (2018).
- [48] C. L. Jia, D. Ma, A. F. Schäffer, J. Berakdar, Twisting the spin wave: on vortices, skyrmions, helical waves and the magnonic spiral phase plate, [arXiv:1909.04457](https://arxiv.org/abs/1909.04457)
- [49] H. Fujita and M. Sato, Ultrafast generation of skyrmionic defects with vortex beams: Printing laser profiles on magnets, *Phys. Rev. B* **95**, 054421 (2017).
- [50] H. Fujita and M. Sato, Encoding orbital angular momentum of light in magnets, *Phys. Rev. B* **96**, 060407(R) (2017).
- [51] F. Garcia-Sanchez, J. Sampaio, N. Reyren, V. Cros, and J.-V. Kim, A skyrmion-based spin-torque nano-oscillator, *New J. Phys.* **18**, 075011 (2016).
- [52] S. Zhang, J. Wang, Q. Zheng, Q. Zhu, X. Liu, S. Chen, C. Jin, Q. Liu, C. Jia, and D. Xue, Current-induced magnetic skyrmions oscillator, *New J. Phys.* **17**, 023061 (2015).
- [53] Z.-X. Li, Y. Cao, X. R. Wang, and P. Yan, Realizing Corner States in Artificial Crystals Based on Topological Spin Textures, [arXiv:1910.03956](https://arxiv.org/abs/1910.03956).
- [54] F. N. Rybakov, A. B. Borisov, S. Blügel, and N. S. Kiselev, New Type of Stable Particlelike States in Chiral Magnets, *Phys. Rev. Lett.* **115**, 117201 (2015).
- [55] F. Zheng, F. N. Rybakov, A. B. Borisov, D. Song, S. Wang, Z.-A. Li, H. Du, N. S. Kiselev, J. Caron, A. Kovács, M. Tian, Y. Zhang, S. Blügel, R. E. Dunin-Borkowski, Experimental observation of chiral magnetic bobbars in B20-type FeGe, *Nat. Nano.* **13**, 451 (2018).
- [56] X. Z. Yu, W. Koshibae, Y. Tokunaga, K. Shibata, Y. Taguchi, N. Nagaosa, and Y. Tokura, Transformation between meron and skyrmion topological spin textures in a chiral magnet, *Nature (London)* **564**, 95 (2018).
- [57] J.-S. B. Tai and I. I. Smalyukh, Static Hopf Solitons and Knotted Emergent Fields in Solid-State Noncentrosymmetric Magnetic Nanostructures, *Phys. Rev. Lett.* **121**, 187201 (2018).
- [58] Y. Liu, R. K. Lake, and J. Zang, Binding a hopfion in a chiral magnet nanodisk, *Phys. Rev. B* **98**, 174437 (2018).
- [59] P. Sutcliffe, Hopfions in chiral magnets, *J. Phys. A* **51**, 375401 (2018).
- [60] F. N. Rybakov, N. S. Kiselev, A. B. Borisov, L. Döring, C. Melcher, and S. Blügel, Magnetic hopfions in solids, [arXiv:1904.00250](https://arxiv.org/abs/1904.00250).
- [61] X. S. Wang, A. Qaiumzadeh, and A. Brataas, Current-Driven Dynamics of Magnetic Hopfions, *Phys. Rev. Lett.* **123**, 147203 (2019).
- [62] V. M. Kontorovich and V. M. Tsukernik, The Gyromagnetic Effect in an Antiferromagnet at Low Temperatures, *Zh. Eksp. Teor. Fiz.* **53**, 1814 (1967) [*Sov. Phys. JETP* **26**, 1035 (1968)].
- [63] H. Y. Yuan and M.-H. Yung, Thermodynamic entanglement of magnonic condensates, *Phys. Rev. B* **97**, 060405(R) (2018).